Journal of Materials Chemistry A

PAPER

Cite this: J. Mater. Chem. A, 2014, 2, 8314

Sandwich-structured graphene–$NiFe_2O_4$–carbon nanocomposite anodes with exceptional electrochemical performance for Li ion batteries

Elham Kamali Heidari,[ab] Biao Zhang,[a] Mahmoud Heydarzadeh Sohi,[b] Abolghasem Ataie[b] and Jang-Kyo Kim*[a]

Received 28th January 2014
Accepted 15th March 2014

DOI: 10.1039/c4ta00507d

www.rsc.org/MaterialsA

Graphene–$NiFe_2O_4$–carbon nanocomposites with a sandwich structure are synthesized *via* the hydrothermal growth of $NiFe_2O_4$ nanoparticles on graphene sheets, followed by carbon coating. As a promising anode material for Li ion batteries, the nanocomposites deliver exceptional cycle stability of 1195 mA h g^{-1} after 200 cycles measured at 500 mA g^{-1}. This value is among the highest reported so far for anodes containing similar $NiFe_2O_4$ nanoparticles. The synergy arising from the conductive graphene substrate, the well-dispersed, ultrafine $NiFe_2O_4$ nanoparticles and the protective carbon layer sustaining the sandwich together is responsible for this trait.

Introduction

Li ion batteries (LIBs) have achieved significant success for application in portable electronics, and there is an increasing demand for further improvement of electrochemical properties, such as power/energy densities, cyclic life and high rate capabilities, for powering next-generation electric vehicles.[1,2] Anode is one of the key components of LIBs, for which graphite has been the dominant source material. However, its low capacity of 372 mA h g^{-1} limits the widespread applications, leading to a search for alternatives with higher energy/power densities.[3] Metal oxides are promising materials to replace graphite anodes due to their ability to react reversibly with Li ions and much higher theoretical capacities.[4] Significant progress has been made in developing high-capacity anode materials using nanostructured metal oxides, such as SnO_2,[5,6] TiO_2 (ref. 7) and $Li_4Ti_5O_{12}$.[8,9] In addition, transition metal ferrites, MFe_2O_4, with a spinel structure are known to be another excellent substitute because the two metal elements can take part in redox reactions and therefore lead to high theoretical capacities.[10] Furthermore, they can possibly tune the energy density and working voltage by varying the metal content.[11] The electrochemical performance of ferrites in their pure form or in composites with other materials, such as Fe_3O_4,[12–14] $CoFe_2O_4$,[15–17] $ZnFe_2O_4$ (ref. 18 and 19) and $MgFe_2O_4$,[20,21] has been extensively studied. Being a member of spinel ferrites, $NiFe_2O_4$ has a high theoretical capacity of 915 mA h g^{-1}, but it suffers from poor cyclic stability owing to the large volume change during Li ion insertion and extraction,[22] like many other metal oxides.

Various strategies have been explored to circumvent the aforementioned obstacles and achieve enhanced electrochemical properties. One strategy is to design different nanostructures that can withstand the volumetric expansion imposed: *e.g.* porous electrode materials[23] or two-dimensional nano-architectures.[24] Another strategy is to combine these metal oxides with nanostructured carbon as the support or substrate.[5,6,24–31] The nanocarbon substrate not only functions as a buffer to relieve the stress arising from the volumetric expansion but also improves the electronic conductivity by offering a 3D conductive network, which is essential for achieving excellent rate capabilities of the electrodes.[32,33] Among many allotropes of carbon, graphene has been proven to be the most desirable carbon substrate for metal oxides due to its extremely large surface area, excellent conductivity, mechanical strength, chemical stability and high theoretical capacity.[6,34,35] However, the large difference in volume expansion between the metal oxides and graphene during the Li ion insertion/extraction may result in a separation of nanoparticles from the graphene substrates after several charge/discharge cycles, leading to early capacity fading.[36] To avoid the detachment of nanoparticles, the metal oxide–graphene nanocomposites were coated with a thin protective layer, such as amorphous carbon.[36–38] The amorphous carbon layer can not only prevent the nanoparticles from peeling off from the graphene sheets but also function as an additional stress buffer and offer a conductive path, so as to improve the cyclic stability and rate capabilities of the composite electrodes.[39]

Herein, we report the facile synthesis of a sandwich nanostructure consisting of $NiFe_2O_4$ nanoparticles filled between the thin, top amorphous carbon layer and the graphene substrate.

[a]Department of Mechanical and Aerospace Engineering, The Hong Kong University of Science and Technology, Clear Water Bay, Hong Kong, P. R. China. E-mail: mejkkim@ust.hk

[b]School of Metallurgy and Materials Engineering, University of Tehran, Tehran, Iran

The morphologies, structures and electrochemical properties of three-component sandwiches were investigated and compared with those of sandwiches without the top carbon layer. The electrodes made from the sandwich nanostructure delivered exceptional specific capacities, excellent cyclic stability and rate capabilities, which to the best of our knowledge, are among the best reported in the literature for $NiFe_2O_4$-based anode materials in LIBs.

Experimental

Materials and methods

GO was prepared using a chemical method according to our previous studies.[40,41] Essentially, natural graphite flakes (supplied by Asbury Carbons, USA) intercalated with H_2SO_4 were thermally expanded at 1050 °C for 30 s to obtain expanded graphite (EG). EG was mixed with H_2SO_4 and $KMnO_4$ and stirred at 60 °C for 24 h. The solution was transferred into an ice bath, and deionized (DI) water and H_2O_2 were poured slowly into the mixture resulting in a colour change of the suspension to light brown. After stirring for 30 min, GO was washed three times using HCl solution (with a water to HCl volume ratio of 9 : 1), followed by washing with DI water until the pH of the solution became about 5–6. The GO thereby obtained was redispersed in ethanol at a concentration of 1 mg ml^{-1}.

A two-step hydrothermal treatment was carried out for *in situ* synthesis of $NiFe_2O_4$ nanoparticles on the surface of graphene oxide (GO), which was coated with glucose as the carbon source and subjected to carbonization to produce composites. Fig. 1 illustrates the synthesis procedure for graphene–$NiFe_2O_4$–carbon (G–NF–C) nanocomposites with a sandwich structure.

Initially, 0.153 g $Ni(NO_3)_2 \cdot 6H_2O$ (Sigma Aldrich) and 0.422 g $Fe(NO_3)_3 \cdot 9H_2O$ (Sigma Aldrich) were mixed with 40 ml GO suspension under vigorous stirring, followed by the drop-wise addition of NH_3 to adjust the pH of the mixture to about 10 and stirred for 1 h. The resulting mixture was transferred into a Teflon-lined stainless steel autoclave and heated to 180 °C for 10 h. After cooling to ambient temperature, the precipitate was centrifuged and washed with DI water and ethanol, and redispersed in 20 ml DI water and sonicated for 20 min. 0.126 g glucose was added to the solution as the carbon source and stirred for 30 min at room temperature. The solution was then transferred to an autoclave and heated to 180 °C for 10 h. The product was centrifuged and washed with DI water several times and dried in a vacuum oven at 60 °C to obtain G–NF–C nanocomposites containing ~20% graphene and ~60% ferrite nanoparticles. The optimal graphene and ferrite nanoparticle contents were determined after extensive preliminary experiments. G–NF composites without the carbon coating were also prepared using the same procedure except the addition of glucose.

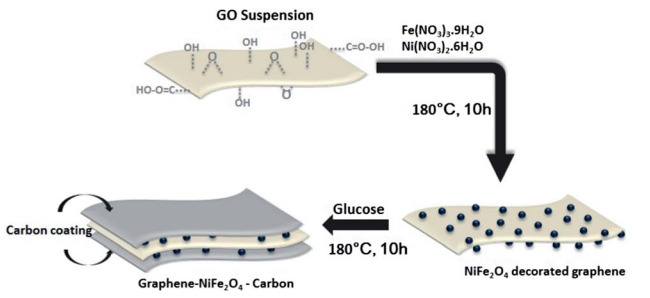

Fig. 1 Illustration of the synthesis procedure for graphene–$NiFe_2O_4$–carbon (G–NF–C) nanocomposites with a sandwich structure.

Structural characterization

X-ray photoelectron spectroscopy (XPS, Surface analysis PHI5600, Physical Electronics) was employed to evaluate the chemical status of the nanocomposites using the Al Kα line as the excitation source. The phase structure of the nanocomposites was determined on a powder X-ray diffraction (XRD) system (PW1830, Philips) with Cu Kα radiation from 10° to 90°. Thermogravimetric analysis (TGA) was conducted (TGA/DTA 92 Setaram II testing system) in air over a temperature range of 50–800 °C at a heating rate of 10 °C min^{-1}. The morphologies of the nanocomposites were investigated using a high-resolution transmission electron microscope (HRTEM, JEOL 2010, 200 kV) and a field emission scanning electron microscope (FESEM, Hitachi S4160).

Electrochemical measurements

The electrochemical tests were carried out using CR 2032 coin cells, according to our previous study.[42] The active material, carbon black and polyvinylidene fluoride (PVDF) as binder were mixed in a weight ratio of 70 : 10 : 20, and a few drops of *N*-methyl-2-pyrrolidone as the solvent was added to form a proper slurry. The slurry was coated onto a copper foil, from which circular pellets having a diameter of 12 mm were cut for use as electrodes. The cells were assembled in an Ar-filled glove box with a Li foil as the counter electrode, $LiPF_6$ (1 M) in ethyl carbonate (EC)–dimethyl carbonate (DMC) (1 : 1 by volume) as the electrolyte and a microporous polyethylene film (Celgard 2400) as the separator. The coin cells were tested between 0 and 3 V and at different current densities on a battery tester (LAND 2001 CT). The cyclic voltammetry (CV) test was performed between 0 and 3 V at a scan rate of 0.001 mV s^{-1}. The specific capacities were calculated based on the weights of the active materials.

Results and discussion

The *in situ* reduction of GO occurring during the hydrothermal treatment and the presence of the carbon coating were confirmed by the XPS spectra, as shown in Fig. 2. The deconvoluted C 1s spectra of the nanocomposites before the hydrothermal treatment, and before and after carbon coating exhibited four peaks corresponding to carbon atoms with different oxygenated functional groups.[36] The G–NF nanocomposites (Fig. 2b) had peaks at 284.6 eV for non-oxygenated C, at 286.2 eV for C–O, at 288 eV for C═O, and at 289.5 eV for O–C═O, respectively.[43] The peaks for the G–NF–C nanocomposites (Fig. 2c) were almost the same as the G–NF results.

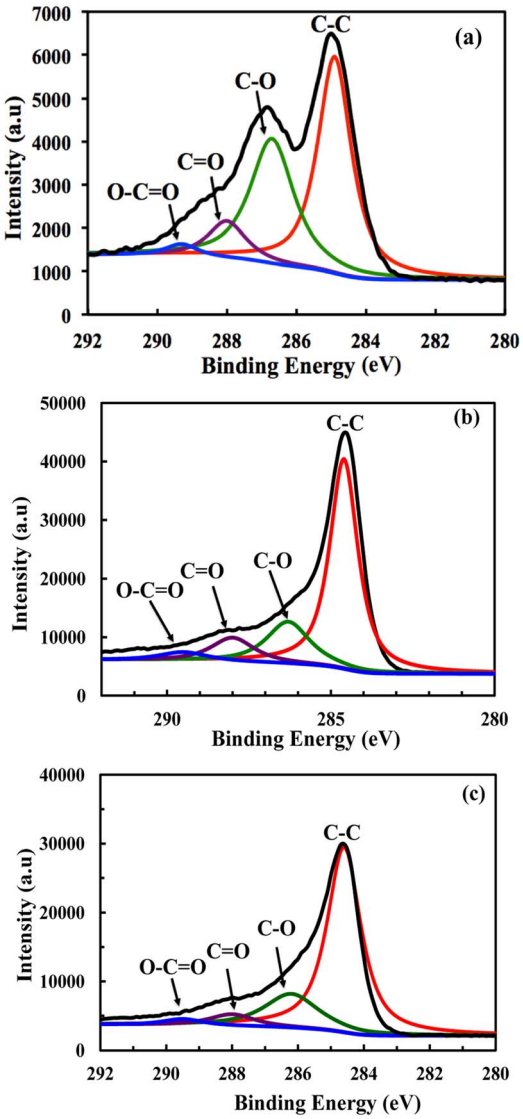

Fig. 2 C 1s XPS spectra of (a) GO–NF, (b) G–NF and (c) G–NF–C nanocomposites.

The peak intensities of the oxygenated groups in both hydrothermally treated composites (Fig. 2b and c) were much lower than those of the GO–NF (Fig. 2a), indicating an effective reduction of GO.[30] The atomic percentage of carbon in G–NF was 49.4%, which increased to 67.0% in G–NF–C. The ratios of non-oxygenated C to oxidized C were calculated by measuring the areas under the peaks after deconvolution (Table 1), revealing a significant increase from 1.64 to 2.42 after carbon coating, a reflection of the higher C–C content in the carbon coating than in graphene.[36]

Table 1 Carbon and oxygenated functional groups in G–NF and G–NF–C nanocomposites

Functional groups	C–C	C–O	C=O	O=C–O	(C–C): (C···O)
Binding energy (eV)	284.6	286.2	288	289.5	
G–NF (at.%)	62.1	23.4	9.8	4.7	1.64
G–NF–C (at.%)	70.7	20.7	5.9	2.7	2.42

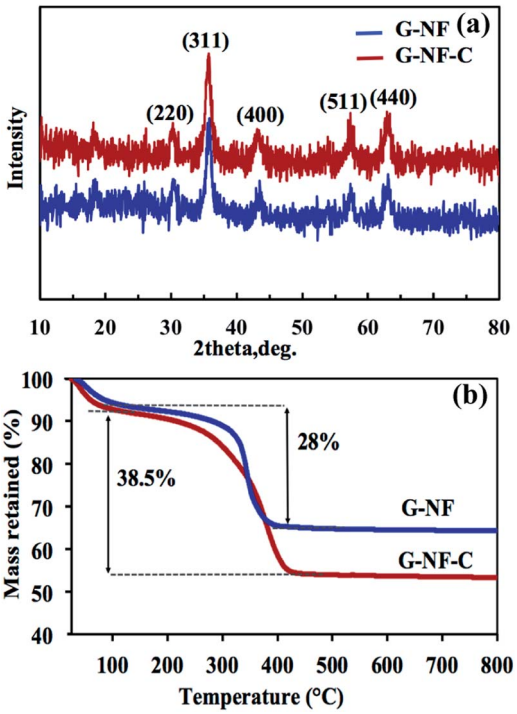

Fig. 3 (a) XRD patterns of G–NF and G–NF–C nanocomposites and (b) TGA analysis of G–NF–C.

Fig. 3a shows the XRD patterns of the G–NF and G–NF–C nanocomposites. The diffraction peaks in both materials were identical and consistent with $NiFe_2O_4$, indicating virtually no effect of carbon coating on the crystalline structure of $NiFe_2O_4$ nanoparticles. The generally broadened peaks in both nanocomposites are a reflection of the formation of very fine $NiFe_2O_4$ nanocrystals. The contents of the $NiFe_2O_4$ nanoparticles and carbon were evaluated using TGA, as shown in Fig. 3b. To obtain the carbon coating content, the ratio of $NiFe_2O_4$ to the graphene content was first measured from the G–NF nanocomposite. There was an initial loss of ~6.5 wt% at 120 °C due to the evaporation of the absorbed solvent. Further heating to above 450 °C resulted in a 28 wt% loss, which was attributed to the oxidation and decomposition of graphene. By subtracting the solvent weight, a weight ratio of graphene : $NiFe_2O_4$ = 3 : 7 was determined. The losses due to the absorbed solvent and the oxidation/decomposition of graphene for the G–NF–C composite were 7.5 and 38.5 wt%, respectively. By taking into account both the solvent weight and the graphene to $NiFe_2O_4$ weight ratio (3 : 7), a net carbon coating content of 16.6 wt% was obtained.

Fig. 4 shows the HRTEM images of G–NF and G–NF–C nanocomposites. The $NiFe_2O_4$ nanoparticles had uniform sizes ranging from 4 to 7 nm and were well distributed on the graphene substrate before (Fig. 4a) and after coating with carbon (Fig. 4b). The thin and almost transparent sheet supporting the NF particles in Fig. 4c suggests a single graphene layer of G–NF. The darker and less transparent substrate in G–NF–C (Fig. 4d)

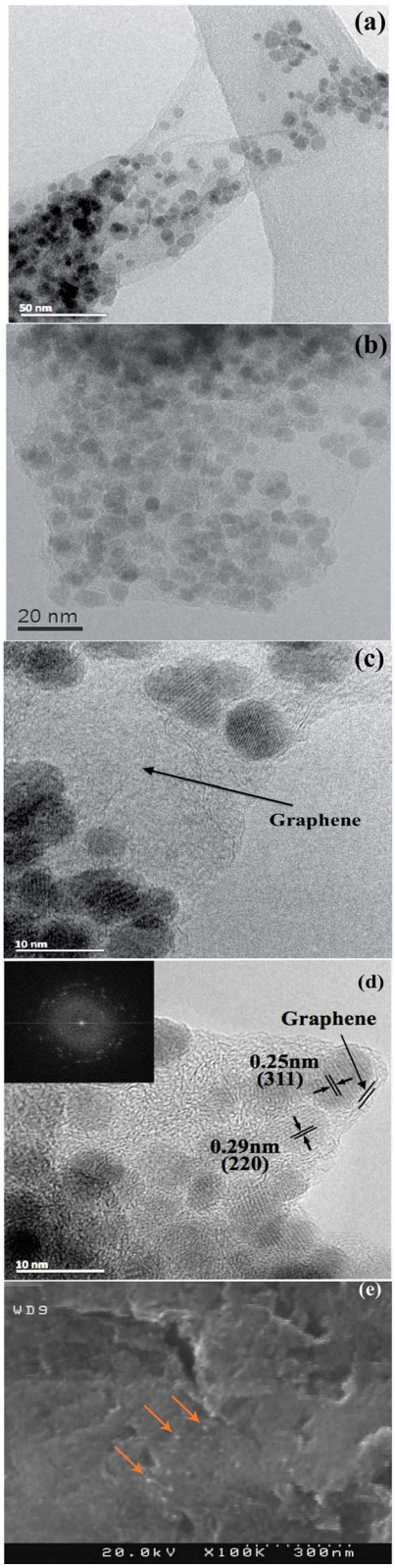

Fig. 4 HRTEM images of (a, c) G–NF and (b, d) G–NF–C nanocomposites with fast Fourier transform (FFT) patterns (in the inset of d); and (e) FESEM image of G–NF–C.

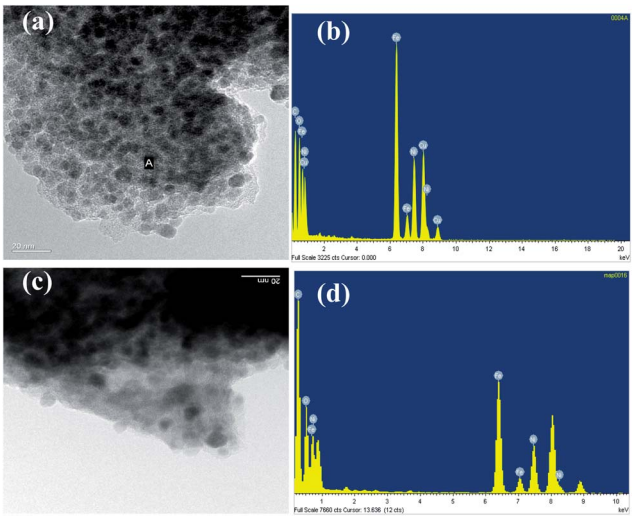

Fig. 5 TEM images and the corresponding EDX profiles of (a, b) G–NF and (c, d) G–NF–C composites.

with an apparently amorphous structure indicates that a carbon layer covered the nanocomposite. The corresponding fast Fourier transform (FFT) patterns in the inset (Fig. 4d) revealed lattice fringe spacings of 0.29 and 0.25 nm that represent the (311) and (220) crystallographic planes of the $NiFe_2O_4$ nanoparticles, respectively. The distribution of NF nanoparticles on the graphene sheets is seen from the FESEM image of G–NF–C (Fig. 4e).

The TEM images and the corresponding energy-dispersive X-ray spectroscopy (EDX) profiles of G–NF (Fig. 5a and b) and G–NF–C composites (Fig. 5c and d) were studied to further verify the existence of carbon coating in G–NF–C. The elemental compositions calculated from the EDX spectra (Table 2) indicate a drastic increase in carbon content after coating, *i.e.* 26 *vs.* 58 at% for G–NF and G–NF–C, respectively.

The results obtained from the electrochemical tests of the electrodes are shown in Fig. 6. The charge/discharge profiles of G–NF–C measured at a current density of 0.1 A g^{-1} with a voltage range 0–3 V (Fig. 6a) reveals that the first discharge saw a voltage quasi-plateau at about 0.8 V, corresponding to the reduction of Ni^{2+} and Fe^{3+} during Li intercalation. The first charge process resulted in a quasi-plateau at about 1.5 V, attributed to oxidation of the transition metals.[28] To investigate the mechanism of reactions between the Li ions and the active material, the cyclic voltammetry (CV) test was carried out (Fig. 6b). The large cathodic peak at 0.55 V is attributed to the

Table 2 Atomic and weight ratios of elements measured by EDX

G–NF			G–NF–C	
Element	Weight%	Atomic%	Weight%	Atomic%
C K	8.38	26.08	27.62	58.01
O K	8.12	18.96	8.69	13.70
Fe K	54.83	36.70	41.40	18.71
Ni K	28.67	18.25	22.29	9.58

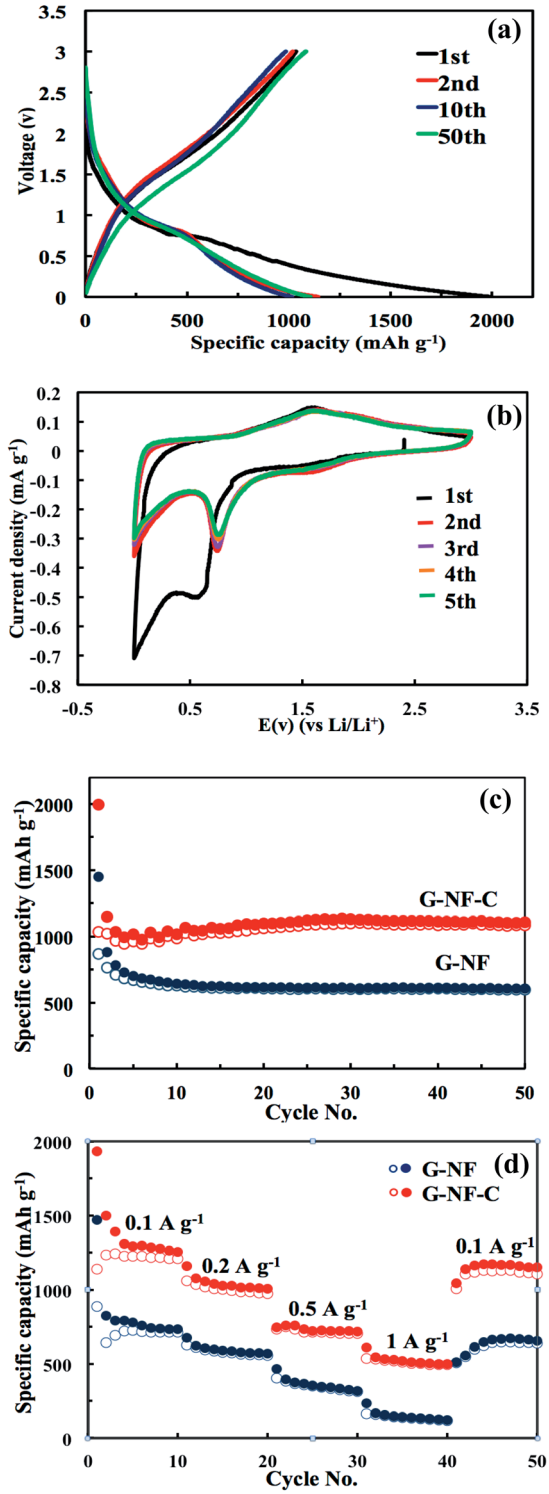

Fig. 6 (a) Charge/discharge profiles of G–NF–C at 0.1 A g^{-1}; (b) cyclic voltammetry curves of G–NF–C in the voltage window of 0.01–3.00 V and scanned at 0.001 mV s^{-1}; (c) cyclic performance of G–NF and G–NF–C electrodes at 0.1 A g^{-1}; and (d) rate performance of G–NF and G–NF–C electrodes at current densities in the range 0.1–1.0 A g^{-1}.

reduction of Fe^{3+} and Ni^{2+} to Fe^0 and Ni^0, respectively, during the first discharge of the $NiFe_2O_4$ nanoparticles. It is shown previously that the first discharge peaks of Fe_2O_3 and NiO appeared at 0.7 and 0.4 V, respectively.[22,44] It is postulated that these two peaks overlapped to form a broad cathodic peak under the current experimental conditions. In the reversible process, the anodic peaks at 1.78 V are ascribed to the oxidation of Ni^0 and Fe^0 to Ni^{2+} and Fe^{3+}, respectively. The electrochemical reversible reactions can be expressed by eqn (1):

$$NiFe_2O_4 + 8e + 8Li \Leftrightarrow Ni^0 + 2Fe^0 + 4Li_2O \quad (1)$$

In the subsequent cycles, the cathodic peak down-shifted to ~0.7 V while the anodic peak up-shifted to ~1.9 V. It is obvious that the CV curves in the subsequent cycles almost completely overlapped, proving excellent cyclic stability.

The cyclic performance of the G–NF and G–NF–C electrodes measured at 0.1 A g^{-1} is shown in Fig. 6c. There were large initial capacity losses for both electrodes, which are considered inevitable due to the formation of a solid electrolyte interface (SEI) on the electrode surface. After the initial large drop, the capacities of the G–NF electrode continued to decrease with increasing cycles, possibly arising from the detachment of the $NiFe_2O_4$ nanoparticles from the graphene substrate caused by the volume changes during the Li ion insertion/extraction. In contrast, the cyclic performance improved significantly after the coating with a carbon layer: the G–NF–C electrode exhibited capacities with a rising trend up to about 30 cycles, which was followed by a very stable cyclic performance. It appears that all the $NiFe_2O_4$ nanoparticles did not initially participate in the reactions with Li ions because of the carbon layer. During the initial 30 cycles, the carbon layer became more permeable to Li ions so that they could penetrate into the underneath $NiFe_2O_4$ nanoparticles, leading to stable cyclic behavior.

The G–NF electrode had a discharge capacity of 1452 mA h g^{-1} in the first cycle, showing a gradual decay of capacity with further cycles before reaching 510 mA h g^{-1} after 50 cycles. The G–NF–C electrode delivered a much higher reversible capacity of 1105 mA h g^{-1} after 50 cycles. The large difference in specific capacity between the two electrodes signifies the important roles that the top carbon layer played. The top coating in the G–NF–C nanocomposites functioned as a shield to prevent the $NiFe_2O_4$ nanoparticles from dropping off from the graphene substrate after debonding. Apart from the mechanical shield, the carbon layer contributed to the capacity of the composite electrode, resulting in a capacity higher than the theoretical value of $NiFe_2O_4$. It also played additional functions as a stress buffer and an electronic conductor, further enhancing the rate capabilities of the composite electrode. Indeed, the rate performance was substantially better for the G–NF–C electrode than the G–NF counterpart for all the current densities studied (Fig. 6d). The relatively higher capacity obtained after 50 cycles at varying current densities (Fig. 6d) than the corresponding capacity after 50 cycles at a constant current density 0.1 A g^{-1} (Fig. 6c) seems to be related to a lesser degree of irreversible capacity degradation due to the less time allowed for the formation of SEI films at higher current densities because time, rather than the number of cycles, is the dominant factor in SEI growth.[45] The difference in specific capacity between the two

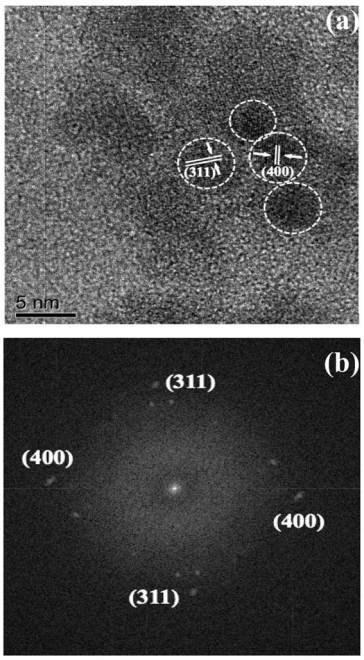

Fig. 7 (a) HRTEM images of G–NF–C nanocomposite electrodes after 50 cycles and (b) the corresponding fast Fourier transform (FFT) electron diffraction pattern.

electrode materials was as large as 600 mA h g^{-1} depending on the current density. The G–NF–C electrode had an excellent capacity over 520 mA h g^{-1} at 1000 mA g^{-1}.

To confirm the stability of the active $NiFe_2O_4$ nanoparticles in the G–NF–C electrode, the changes in their morphology were examined after 50 cycles under an HRTEM, as shown in Fig. 7. The $NiFe_2O_4$ nanoparticles maintained their uniform distribution (Fig. 7a), confirming the intact protection offered by the top carbon layer and the graphene substrate. The nanoparticles maintained their original uniform sizes in the range of 4–7 nm, proving the little damage caused by the Li ion insertion/extraction cycles. The lattice fringe spacings of 0.25 and 0.21 nm also matched well with the (311) and (400) planes, respectively, of the $NiFe_2O_4$ nanoparticles. The fast Fourier transform (FFT) electron diffraction pattern (Fig. 7b) further demonstrates excellent crystallinity of the nanoparticles even after many cycles. In summary, it can be concluded that the carbon top layer was proven to be very effective in protecting the $NiFe_2O_4$ nanoparticles to maintain their original crystalline structure, thus capable of sustaining the high electrochemical stability of the active material.

To track the chemical changes in active materials after they underwent a certain number of cycles, XPS studies of the G–NF–C electrode were carried out after 50 cycles; their results were compared with those of the pristine electrode (Fig. 8). It is worth noting that both Fe 2p and Ni 2p peaks disappeared after the cycles (Fig. 8a and b), a reflection of the coverage of the active material by a solid electrolyte interface (SEI) film as the reaction product between the electrode and the electrolyte solution. The SEI film was responsible for the large difference in discharge capacity between the first cycle and the following cycles. The C

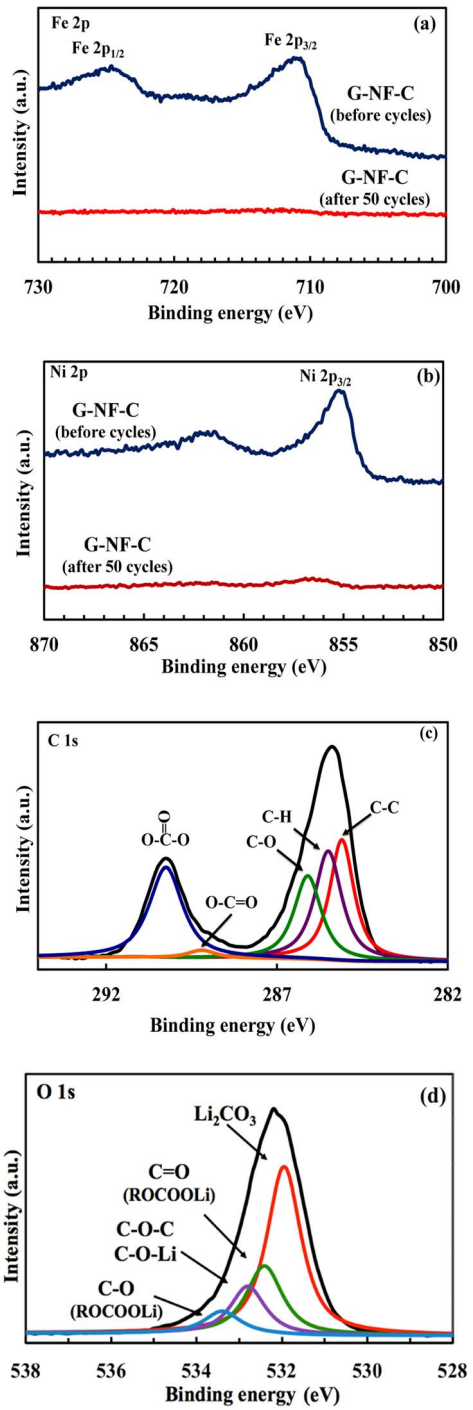

Fig. 8 Comparison of (a) Fe 2p and (b) Ni 2p XPS spectra of G–NF–C electrodes between before and after 50 cycles at 0.1 A g^{-1}; and (c) C 1s and (d) O 1s deconvoluted XPS spectra of G–NF–C electrode after 50 cycles.

1s and O 1s deconvoluted peaks for the cycled electrodes were used to identify the composition of the SEI film. The C 1s spectrum consisted of two main peaks at 285.5 and 290.2 eV (Fig. 8c). The peak at 290.2 eV was attributed to carbon atoms bonded to the oxygen atoms in lithium alkyl carbonates (R–C–

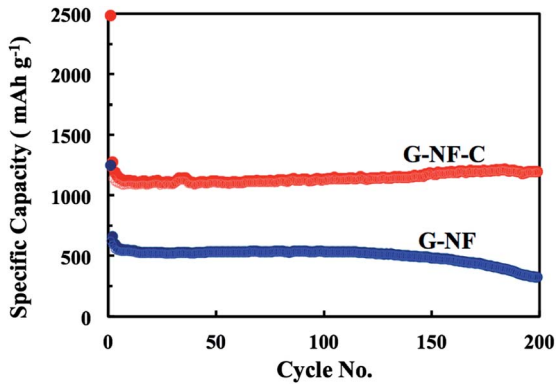

Fig. 9 Cyclic performance of G–NF and G–NF–C composite electrodes at 0.5 A g^{-1}.

O–COOLi) and Li_2CO_3, indicating that these species were the main components of the SEI film.[9,46,47] The O 1s spectrum (Fig. 8d) was deconvoluted into four peaks where the most prominent peak at 531.9 eV was attributed to the oxygen bonds in Li_2CO_3, and the peak at 533.5 eV represents lithium alkyl carbonate.

To evaluate the long-term cyclic performance, the capacities of the electrodes with and without the carbon coating were measured at 0.5 A g^{-1} for 200 cycles, as shown in Fig. 9. The G–NF electrode presented a capacity of 520 mA h g^{-1} after 120 cycles, followed by rapid decay to 317 mA h g^{-1} at the 200th cycle. In contrast, the G–NF–C electrode delivered a very stable cyclic performance with an exceptional capacity of 1195 mA h g^{-1} even after 200 cycles. This value is considered, to the authors' best knowledge, among the highest and the most stable capacities reported so far for anodes containing similar $NiFe_2O_4$ nanoparticles. Table 3 presents a comparison of the capacities of $NiFe_2O_4$-based anode materials between the current study and the literature findings.

The excellent electrochemical performance of the G–NF–C anode arose from the synergistic effects of graphene and carbon coating. The graphene layer functioned as a conductive substrate to facilitate the ion/electron transport and served as a buffer to relieve the stress. An additional important role that the graphene substrate played was to discourage the excessive growth and agglomeration of $NiFe_2O_4$ nanoparticles during the synthesis process.[34] The small particle size was advantageous because it can maintain a large surface area, thus providing large sites for Li ion reaction. Even with all these advantages of graphene, the G–NF electrode became unreliable after long cycles because of the inevitable separation of nanoparticles from the graphene layer due to the large difference in the volume change between them. Excellent long cyclic stability in electrochemical performance was achieved after introducing the carbon layer on the surface of the nanocomposite. The carbon coating served as a shield to inhibit the separation of $NiFe_2O_4$ nanoparticles from the graphene substrate even after long cycles, in addition to contributing to the capacity and acting as an additional stress buffer and conducting layer, as discussed above.

Conclusion

Sandwich-structured G–NF–C nanocomposites were synthesized *via* hydrothermal growth of $NiFe_2O_4$ nanoparticles on a graphene substrate and the glucose-derived carbon coating. Benefiting from the sandwich structure, the electrode made from the three-component composites showed significantly improved cyclic stability compared with those without the carbon coating. The G–NF–C electrode delivered an exceptional specific capacity of 1195 mA h g^{-1} after 200 cycles at a high rate of 500 mA g^{-1}, whereas the G–NF electrode showed a moderate capacity of 520 mA h g^{-1} after 120 cycles at the same current density. The much better electrochemical performance of the G–NF–C electrode than the G–NF counterpart was attributed to the top carbon coating that not only served as an additional active material and stress buffer and electronic conductive layer, but also functioned as a shield to prevent the detachment of $NiFe_2O_4$ nanoparticles from the graphene substrate even after long cycles.

Table 3 Comparison of specific capacities of $NiFe_2O_4$ (NF)-based anode materials developed in this study with literature data

Material	Current rate	Cycle no.	Specific capacity [mA h g^{-1}]	Ref.
G–NF–C	500 mA g^{-1}	200	1195	Current study
G–NF	500 mA g^{-1}	120	520	
G–NF (20 : 80) (hydrothermal)	100 mA g^{-1}	50	812	10
NF nanofiber	100 mA g^{-1}	40	870	48
		100	1000	
NF nanoparticles	100 mA g^{-1}	50	550	48
NF nanorod	1000	300	520	49
NF–C	1/8 C	40	780	50
	4 C	40	200	
NF nanoparticles (5–15 nm)	0.2 mA cm^{-2}	3	709	22
NF (30 nm)	0.2 mA cm^{-2}	10	600	51
NF (double layer hydroxide precursor)	1/8 C	20	470	52
NF (sol–gel method)	1 C	80	600	53

Acknowledgements

This project was supported by the Research Grants Council of the Hong Kong SAR (Project codes: 613811 and 613612). The authors also appreciate the technical assistance from the Materials Characterization and Preparation Facilities (MCPF) of HKUST. E.K.H. was a visiting PhD student at HKUST from the University of Tehran under the SENG Visiting Internship Program of HKUST when this work was done. The authors appreciate the support from University of Tehran under the research scheme no. 8107024/1/02.

References

1 N. Mahmood, C. Zhang, H. Yin and Y. Hou, *J. Mater. Chem. A*, 2014, **2**, 15.
2 I. R. M. Kottegoda, N. H. Idris, L. Lu, J. Z. Wang and H. K. Liu, *Electrochim. Acta*, 2011, **56**, 5815.
3 A. K. Rai, L. T. Anh, J. Gim, V. Mathew, J. Kang, B. J. Paul, N. K. Singh, J. Song and J. Kim, *J. Power Sources*, 2013, **244**, 435.
4 P. Poizot, S. Laruelle, S. Grugeon, L. Dupont and J. M. Tarascon, *Nature*, 2000, **407**, 496.
5 B. Zhang, Y. Yu, Z. D. Huang, Y. B. He, D. H. Jang, W. S. Yoon, Y. W. Mai, F. Kang and J. K. Kim, *Energy Environ. Sci.*, 2012, **5**, 9895.
6 B. Zhang, Q. B. Zheng, Z. D. Huang, S. W. Oh and J. K. Kim, *Carbon*, 2011, **49**, 4524.
7 Y. B. He, M. Liu, Z. L. Xu, B. Zhang, B. Li, F. Kang and J. K. Kim, *Energy Technol.*, 2013, **1**, 668.
8 B. Zhang, Y. Liu, Z. D. Huang, S. W. Oh, Y. Yu, Y. W. Mai and J. K. Kim, *J. Mater. Chem.*, 2012, **22**, 12133.
9 Y. B. He, M. Liu, Z. D. Huang, B. Zhang, Y. Yu, B. Li, F. Kang and J. K. Kim, *J. Power Sources*, 2013, 1.
10 Y. Fu, Y. Wan, H. Xia and X. Wang, *J. Power Sources*, 2012, **213**, 338.
11 M. Li, Y. X. Yin, C. Li, F. Zhang, L. J. Wang, S. Xu and D. G. Evans, *Chem. Commun.*, 2012, **48**, 410.
12 H. Wu, N. Du, J. Wang, H. Zhang and D. Yang, *J. Power Sources*, 2014, **246**, 198.
13 P. Lian, S. Liang, X. Zhu, W. Yang and H. Wang, *Electrochim. Acta*, 2011, **58**, 81.
14 H. Xia, Y. Wan, G. Yuan, Y. Fu and X. Wang, *J. Power Sources*, 2013, **241**, 486.
15 H. Xia, D. Zhu, Y. Fu and X. Wang, *Electrochim. Acta*, 2012, **83**, 166.
16 Y. Q. Chu, Z. W. Fu and Q. Z. Qin, *Electrochim. Acta*, 2004, **49**, 4915.
17 M. Zhang, Y. Jin, Q. Wen, C. Chen and M. Jia, *Appl. Surf. Sci.*, 2013, **277**, 25.
18 Y. Sharma, N. Sharma, G. V. S. Rao and B. V. R. Chowdari, *Electrochim. Acta*, 2008, **53**, 2380–2385.
19 W. Song, J. Xie, Sh. Liu, G. Cao, T. Zhu and X. Zhao, *New J. Chem.*, 2012, **36**, 2236.
20 Y. Pan, Y. Zhang, X. Wei, C. Yuan, J. Yin, D. Cao and G. Wang, *Electrochim. Acta*, 2013, **109**, 89.
21 N. Sivakumar, S. R. P. Gnanakan, K. Karthikeyan, S. Amaresh, W. S. Yoon, G. J. Park and Y. S. Lee, *J. Alloys Compd.*, 2011, **509**, 7038.
22 H. Zhao, Z. Zheng, K. W. Wong, S. Wang, B. Huang and D. Li, *Electrochem. Commun.*, 2007, **9**, 2606.
23 A. Vu, Y. Qian and A. Stein, *Adv. Energy Mater.*, 2012, **2**, 1056.
24 J. Liu and X. W. Liu, *Adv. Mater.*, 2012, **24**, 4097.
25 D. J. Xue, S. Xin, Y. Yan, K. C. Jiang, Y. X. Yin, Y. G. Guo and L. J. Wan, *J. Am. Chem. Soc.*, 2012, **134**, 2512.
26 Z. Liang, R. Huo, S. Yin, F. Zhang and S. Xu, *J. Mater. Chem. A*, 2014, **2**, 921.
27 X. Zhou, Y. X. Yin, A. M. Cao, L. J. wan and Y. G. Guo, *ACS Appl. Mater. Interfaces*, 2012, **4**, 2824.
28 H. D. Oh, S. W. Lee, S. O. Kim and J. K. Lee, *J. Power Sources*, 2013, **244**, 575.
29 L. Wu, Q. Xiao, Z. Li, G. Lei, P. Zhang and L. Wang, *Solid State Ionics*, 2012, **215**, 24.
30 C. Gong, Y. J. Bai, Y. X. Qi, N. Lun and J. Feng, *Electrochim. Acta*, 2013, **90**, 119.
31 F. Mueller, D. Bresser, E. Paillard, M. Winter and S. Passerini, *J. Power Sources*, 2013, **236**, 87.
32 Y. Yu, Y. Zhu, H. Gong, Y. Ma and X. Zhang, *Electrochim. Acta*, 2012, **83**, 53.
33 X. M. Liu, Z. D. Huang, S. W. Oh, B. Zhang, P. C. Ma, M. F. Yuen and J. K. Kim, *Compos. Sci. Technol.*, 2012, **72**, 121.
34 Z. S. Wu, G. Zhou, L. H. Yin, W. Ren, F. Li and H. M. Cheng, *Nano Energy*, 2012, **1**, 107.
35 B. Zhang, Y. Yu, Y. S. Liu, Z. D. Huang, Y. B. He and J. K. Kim, *Nanoscale*, 2013, **5**, 2100.
36 C. Zhang, X. Peng, Z. Guo, C. Cai, Z. Chen, D. Wexler, S. Li and H. Liu, *Carbon*, 2012, **50**, 1897.
37 D. Wang, J. Yang, X. Li, D. Geng, R. Li, M. Cai, T. K. Sham and X. Sun, *Energy Environ. Sci.*, 2013, **6**, 2900.
38 Z. D. Huang, S. W. Oh, Y. B. He, B. Zhang, Y. Yang, Y. W. Mai and J. K. Kim, *J. Mater. Chem.*, 2012, **22**, 19643.
39 D. Li, K. Seng, D. Shi, Z. Chen, H. K. Liu and Z. Guo, *J. Mater. Chem. A*, 2013, **1**, 14115.
40 Y. Geng, S. J. Wang and J. K. Kim, *J. Colloid Interface Sci.*, 2009, **336**, 592.
41 Q. B. Zheng, W. H. Ip, X. Y. Lin, N. Yousefi, K. K. Yeung, Z. G. Li and J. K. Kim, *ACS Nano*, 2011, **5**, 6039.
42 B. Zhang, Z. L. Xu, S. Abouali, M. Akbari, Y. B. He, F. Kang and J. K. Kim, *Adv. Energy Mater.*, DOI: 10.1002/aenm.201301448.
43 J. F. Moulder, W. F. Stickle, P. E. Sobol and K. D. Bomben, *Handbook of X-ray Photoelectron Spectroscopy*, Physical Electronics, Inc., Eden Prairie, MN, USA, 1995.
44 Y. N. NuLi and Q. Z. Qin, *J. Power Sources*, 2005, **142**, 292.
45 S. S. Zhang, K. Xu and T. R. Jow, *J. Power Sources*, 2004, **130**, 281.
46 R. Dedryvère, S. Laruelle, S. Grugeon, L. Gireaud, J. M. Tarascon and D. Gonbeaua, *J. Electrochem. Soc.*, 2005, **152**, 689.
47 S. Leroy, F. Blanchard, R. Dedryvère, H. Martinez, B. Carré, D. Lemordant and D. Gonbeau, *Surf. Interface Anal.*, 2005, **37**, 773.

48 C. T. Cherian, J. Sundaramurthy, M. V. Reddy, P. S. Kumar, K. Mani, D. Pliszka, Ch. H. Sow, S. Ramakrishna and B. V. R. Chowdari, *ACS Appl. Mater. Interfaces*, 2013, **5**, 9957.
49 N. Wang, H. Xu, L. Chen, X. Gu, J. Yang and Y. Qian, *J. Power Sources*, 2014, **247**, 163.
50 Y. Ding, Y. Yang and H. Shao, *J. Power Sources*, 2013, **244**, 610.
51 H. Liu, H. Zhu and H. Yang, *Mater. Res. Bull.*, 2013, **48**, 1587.
52 X. D. Li, W. S. Yang, F. Li, D. G. Evans and X. Duan, *J. Phys. Chem. Solids*, 2006, **67**, 1286.
53 P. Lavela and J. L. Tirado, *J. Power Sources*, 2007, **172**, 379.